Kinking facilitates grain nucleation and modifies crystallographic preferred orientations during high-stress ice deformation

Sheng Fan[1], David J. Prior[1], Travis F. Hager[2], Andrew J. Cross[2,3], David L. Goldsby[2], Marianne Negrini[1]

[1] Department of Geology, University of Otago, Dunedin, New Zealand
[2] Department of Earth and Environmental Science, University of Pennsylvania, Philadelphia, PA, USA
[3] Department of Geology and Geophysics, Woods Hole Oceanographic Institution, Woods Hole, MA, USA

Correspondence to: Sheng Fan (sheng.fan@otago.ac.nz).

Corresponding author: Sheng Fan

Email: sheng.fan@otago.ac.nz

Address: Department of Geology, University of Otago, 360 Leith Street, Dunedin, New Zealand

Phone: +64 21 08842396

Email addresses for co-authors

David J. Prior: david.prior@otago.ac.nz

Travis F. Hager: thager94@gmail.com

Andrew J. Cross: across@whoi.edu

David L. Goldsby: dgoldsby@sas.upenn.edu

Marianne Negrini: marianne.negrini@otago.ac.nz

This paper is a non-peer reviewed preprint, which has been submitted to Earth and Planetary Science Letters for peer review.

Abstract Kinking can accommodate significant amounts of strain during crystal plastic deformation under relatively large stresses and may influence the mechanical properties of cold planetary cryosphere. To better understand the origins, mechanisms, and microstructural effects of kinking, we present detailed microstructural analyses of coarse-grained ice (~1300 µm) deformed under uniaxial compression at -30°C. Microstructural data are generated using cryogenic electron backscattered diffraction (cryo-EBSD). Deformed samples have bimodal grain size distributions, with thin and elongated (aspect ratio ≥ 4) kink domains that develop within, or at the tips of, remnant original grains (≥ 300 µm, aspect ratio < 4). Small, equiaxed subgrains also develop along margins of remnant grains. Moreover, many remnant grains are surrounded by fine-grained mantles of small, recrystallized grains (< 300 µm, aspect ratio < 4). Together, these observations indicate that grain nucleation is facilitated by both kinking and dynamic recrystallization (via subgrain rotation). Low- (< 10°) and high-angle (mostly > 10°, many > 20°) kink bands within remnant grains have misorientation axes that lie predominantly within the basal plane. Moreover, previous studies suggest the kinematics of kinking and subgrain rotation should be fundamentally the same. Therefore, progressive kinking and subgrain rotation should be crystallographically controlled, with rotation around fixed misorientation axes. Furthermore, the *c*-axes of most kink domains are oriented sub-perpendicular to the sample compression axis, indicating a tight correlation between kinking and the development of crystallographic preferred orientation. Kink band densities are the highest within remnant grains that have basal planes sub-parallel to the compression axis (i.e., *c*-axes perpendicular to the compression axis)—these data are inconsistent with models suggesting that, if kinking is the only strain-accommodating process, there should be higher kink band densities within grains that have basal planes oblique to the compression axis (for low kink-host misorientation angles, e.g., ≤ 20°, as in this study). One way to rationalize this inconsistency between kink models and experimental observations is that kinking and dynamic recrystallization are both active during deformation, but their relative activities depend on the crystallographic orientations of grains. For grains with basal planes sub-parallel to the compression axis, strain-induced GBM is inhibited, and large intragranular strain incompatibilities can be relaxed via kinking, when other processes such as subgrain rotation recrystallization are insufficient. For grains with basal planes oblique to the compression axis, strain-induced grain boundary migration (GBM) might be efficient enough to relax the strain incompatibility via selective growth of these grains, and kinking is therefore less important. For grains with basal planes sub-perpendicular to the compression axis, kink bands are seldom observed—for these grains, the minimum shear stress required for kinking exceeds the applied compressive stress, such that kinks cannot nucleate.

1 Introduction

Plastic deformation, accommodated by the high temperature creep of rocks and minerals (including ice), is necessary for many geodynamic phenomena on the Earth and other planetary bodies (Durham and Stern, 2001), including subduction, mountain building, mantle convection, and glacial flow. Microstructural studies and numerical models show that high temperature plastic deformation is facilitated by dynamic recovery and recrystallization (Means, 1983; Urai et al., 1986), which counteract work hardening and give rise to mechanical weakening by minimizing the strain energy associated with crystal defects, e.g., dislocations (Derby and Ashby, 1987; Duval, 1979; Humphreys et al., 2017; Weertman, 1983). Dislocations tend to arrange themselves into low-energy configurations through the process of dynamic recovery. Recovery often produces low-angle intragranular boundaries (subgrain walls), whose misorientation increases as dislocations with the same polarity are added (Humphreys et al., 2017). Recrystallization, on the other hand, involves the creation and/or migration of grain boundaries (Poirier and Guillopé, 1979), which often give rise to grain nucleation via two common processes: grain boundary bulging and subgrain rotation (Urai et al., 1986). Bulge nucleation occurs when a grain boundary segment bulges (i.e., migrates) into a neighbouring grain, typically to sweep out a region of high strain energy (i.e., high defect density). The grain boundary bulge may then be severed by either continued grain boundary migration or by the formation of a subgrain wall across the bulge neck, which becomes increasingly misoriented until it develops into a grain boundary (Halfpenny et al., 2006). Subgrain rotation recrystallization, on the other hand, occurs solely via the progressive misorientation of subgrain walls, which eventually become high-angle boundaries (at a misorientation of roughly ≥10°; Drury and Pennock, 2007) to form a new, distinct grain.

Both bulging and subgrain rotation recrystallization, then, involve the nucleation of new, low-strain recrystallized grains at the expense of original, high-strain remnant grains. Furthermore, models based on experimental observations suggest that recrystallized grains should initially have equiaxed shapes (Halfpenny et al., 2006; Hasegawa and Fukutomi, 2002; Urai et al., 1986). However, rocks deformed at high stresses may become subdivided by two additional processes—twinning and kinking—which produce elongate, blocky domains encompassed by straight boundaries (Nishikawa and Takeshita, 1999). Although twinning and kinking produce similar domain morphologies, they are fundamentally different. Twinning yields a specific crystallographic relationship—i.e., a specific misorientation axis-angle pair—between the parent grain and twin domains (see review by Vernon, 2018). Kinking, on the other hand, produces sharp lattice bending without a specific misorientation axis/angle (Seidemann et al., 2020; Vernon, 2018). Nevertheless, some orientations are more prone to kinking than others.

Numerous studies have been carried out to understand the mechanics of kinking during plastic deformation (e.g., Bell et al., 1986; Gay and Weiss, 1974; Honea and Johnson, 1976; Nishikawa and Takeshita, 1999; Seidemann et al., 2020). These studies reveal that kinking is more prevalent in materials with strong mechanical (elastic and viscous) anisotropy (Barsoum, 2020). For example, Gay and Weiss (1974) found that kinking is controlled by the magnitude of shear stress resolved on easy-slip planes (e.g., the basal plane for ice and quartz)—that is, grains in hard slip orientations are more prone to kinking. Such a relationship was quantified further by Honea and Johnson (1976) and Nishikawa and Takeshita (1999), who modelled the high-stress deformation of elastic multilayers and quartz, respectively. These modelling works show the critical (minimum) shear stress required for the activation of kinking is dependent on the relatively orientation between the crystallographic basal plane and the compression axis: the critical stress is the highest when basal plane is perpendicular to parallel to compression, and it is the lowest when basal plane is at 45° to compression. Using transmission electron microscopy (TEM), Bell and others (1986) proposed that kinking in mica develops via continuous crystal lattice bending due to the progressive addition of dislocations to kink walls, similar to the process of subgrain rotation (Poirier and Nicolas, 1975; Urai et al., 1986).

As a mechanically anisotropic mineral (Duval et al., 1983), the hexagonal form of water ice—ice-1h—is also prone to kinking. Under relatively fast strain rates and/or large differential stresses, ice-1h often develops straight kink boundaries with both low and high misorientation angles, and misorientation axes lying predominantly within the basal (0001) plane (Piazolo et al., 2015; Seidemann et al., 2020). To date, most studies on kinking in ice have focused on the structures of boundaries and the dislocations that comprise them, based on misorientation and Burgers vector analyses (e.g., Piazolo et al., 2015; Seidemann et al., 2020). Seidemann and others (2020) also correlated the activity of kinking (i.e., the number of kink boundaries per grain) with the magnitude of differential stress, using synthetic polycrystalline ice-1h samples deformed under relatively large differential stresses (2.7–13.3 MPa). These observations indicate that kinking should play a key role in accommodating plastic deformation under high stress conditions. Though such conditions are rarely found on Earth—indeed, kinks are seldom reported in terrestrial warm polar ice samples (Jansen et al., 2016; Weikusat et al., 2017)—kinking may play a crucial role in accommodating plastic deformation in the icy lithospheres of other planetary bodies (e.g., Europa, Ganymede, Callisto, Titan) where ice is subjected to larger stresses and lower temperatures (see review by Journaux et al., 2020). However, we still lack a complete understanding of how kinking contributes to grain nucleation and the development of anisotropy (i.e., crystallographic preferred orientation, CPO), especially in ice. This is largely because previous studies focused on relatively fine-grained (~300 μm) ice samples deformed to large strains (> ~20%) (e.g., Seidemann et al., 2020). Even with state-of-the-art quantitative microscopy (e.g., cryogenic electron backscatter diffraction; Prior et al., 2015) it is difficult to resolve intragranular substructures at a resolution finer than ~5 μm in ice. Furthermore, features arising from nucleation due to kinking—e.g., thin, elongate grains—might be overprinted by subsequent plastic deformation and dynamic recrystallization at large strains.

In this contribution, we present microstructural analyses of coarse-grained (~1300 μm) ice samples deformed under uniaxial compression to ~10% strain at -30°C. Samples were deformed under different strain rates in order to test the influence of stress on the development of kinking-related structures. Using coarse-grained ice samples increases our ability to characterise local, intragranular deformation features. Our objectives are to study: (1) the origins (e.g., crystallographic controls) on intragranular (kink) boundary formation, (2) kinking as a grain nucleation process; and (3) the role of kinking in modifying bulk CPOs. By answering these questions, we aim to better understand the cryo-tectonics of icy satellites, as well as the high-stress deformation of terrestrial analogues such as quartz.

2 Method

2.1 Sample fabrication

Ice samples were fabricated using a flood-freeze method (Cole, 1979). Ice seeds with a particle size between 1.6 and 2 mm were produced by sieving crushed ice cubes frozen from deionized ultra-pure water. After that, the ice seeds were "wet sieved" by pouring liquid nitrogen over the ice seeds while sieving. Wet sieving helps to remove fine grains that electrostatically clump together—coarse-grained ice samples produced by dry sieving method contain a significant population of unwanted fine grains (e.g., Qi et al., 2017). Ice seeds were packed into cylindrical moulds with an inner diameter of 25.4 mm. The packed moulds were evacuated to a near-vacuum state and equilibrated in a water ice bath (0°C) for ~40 minutes before being flooded with degassed deionized ultra-pure water at 0°C. The flooded moulds were immediately transferred to a -30°C chest freezer and placed vertically into cylindrical holes in a polystyrene block, with the base of moulds touching a copper plate at the bottom of the freezer. This procedure ensures the freezing front migrates upwards, minimizing any trapping of bubbles within the samples. After 24 hours, the ice samples were gently pushed out from the moulds using an Arbor press. Ice samples were cut and polished on both ends to limit their lengths to 1.5–2.0 times the sample diameter and to ensure that both ends were flat and perpendicular to the sample cylindrical axis. Initial sample lengths were measured using a caliper. Each sample was encapsulated in a thin-walled indium jacket tube (~0.38 mm wall thickness) with the bottom already welded to a stainless-steel end-cap. The top of indium jacket tube was then welded to a steel semi-internal force gauge, with a zirconia spacer placed between the force gauge and sample to thermally insulate the sample during welding. During welding, the sample was kept submerged in a -60°C ethanol bath.

2.2 Experimental set up and process

Uniaxial compression experiments were conducted in a cryogenic, triaxial gas-medium apparatus (Heard et al., 1990) housed in the Ice Physics Laboratory, University of Pennsylvania. The ice samples were uniaxially deformed at -30°C, and at a nitrogen gas pressure of ~40 MPa, under constant displacement rates yielding true axial strain rates of ~1×10^{-5}, 3×10^{-5} and $6 \times 10^{-5} s^{-1}$ that correspond to the uniaxial stresses greater than ~5 MPa (Table 1). Experiments were terminated once the true axial strain reached ~10%. After deformation, samples were extracted from the apparatus within ~15 minutes. To minimize thermal cracking, samples were progressively cooled to ~-30, -100 and -196°C over a further period of ~15 minutes, and thereafter stored in a liquid nitrogen dewar. Minor static recovery of ice microstructures may happen on this timescale (Hidas et al., 2017), but significant changes in CPO and/or grain size are unlikely.

2.3 Cryo-EBSD data

Ice samples were prepared following published procedures for cryogenic electron backscatter diffraction (cryo-EBSD) data collection (Prior et al., 2015). Cryo-EBSD data provide full crystallographic orientations, and microstructural details down to 5 μm spatial resolution in this study. Sample were first cut in a -20°C cold room using a band saw. During this step, samples were stored in ~-100°C liquid nitrogen mist when not being cut. Ice samples were cut in half along the cylinder axis, and a 5-mm thick slice was extracted from half of the sample. The other half of each sample was returned to the liquid nitrogen dewar for archive storage. Cutting time for each sample was <5 minutes. One side of each ice slice, at a temperature of -30 to -50°C, was placed against a copper ingot at ~5°C, forming a bond. Ice-ingot assemblies were immediately returned to the liquid nitrogen mist once fully bonded. Polished sample surfaces were subsequently acquired by hand lapping at ~-40°C on sandpapers with grit sizes of 80, 240, 600, 1200 and 2400. After polishing, ice-ingot assemblies were stored at liquid nitrogen temperature before being transferred to a scanning electron microscope (SEM) for cryo-EBSD data acquisition.

We collected EBSD data from the polished surface of each ice sample. A Zeiss Sigma VP FEG-SEM combined with an Oxford Instruments' Symmetry EBSD camera was used for the data collection. The ice-ingot assembly was transferred to a cold SEM stage maintained at ~-100°C. Pressure cycling in the SEM chamber was performed to remove frost and create a damage-free sample surface via sublimation (Prior et al., 2015). Raw EBSD data were collected with a step size of 5 μm at a stage temperature of ~-95°C, with 2–5 Pa nitrogen gas pressure, 30kV accelerating voltage and ~60 nA beam current.

EBSD maps were indexed (as ice-1h) at a typical rate of ≥90%. Raw EBSD data were montaged using the Oxford Instruments' Aztec software.

2.4 Processing of the cryo-EBSD data

Ice grains were constructed from raw EBSD pixel maps using the MTEX toolbox (Bachmann et al., 2011) with a grain boundary misorientation angle threshold of 10°. Grain size was calculated as the diameter of a circle with area equal to the measured area of each grain. We first removed grains with diameters <20 μm, as they are likely to result from mis-indexing. Poorly-constrained grains (i.e., grains with <50% indexed pixel coverage) were also removed. Next, we applied the MTEX *fill* function, which interpolates non-indexed pixels using a nearest-neighbour method—each non-indexed pixel is replaced by a pixel with the same orientation as its nearest indexed pixel. After that, we reconstructed grains using the interpolated EBSD data. Grains at the edges of EBSD maps were removed. High-angle boundaries are located where the misorientation between neighbouring pixels is >10°. Low-angle boundaries were also calculated using a misorientation angle of 4–10° between neighbouring pixels. In this study, boundaries with misorientation angles <4° were not included in any analyses, since very low angle misorientations produce large uncertainties in misorientation axis orientations (Prior, 1999) . In this study, we measured two parameters that are commonly used to examine grain shape—aspect ratio and shape preferred orientation (SPO). Aspect ratio is defined as the quotient between the long and short axis lengths of an ellipse (convex hull) fitted to each grain. SPO measures the distribution of angles between a given vector (i.e., the compression (y) axis in this study) and the long axis of each grain.

2.4.1 Montage artefacts

During EBSD data acquisition, large area maps were acquired by combining >120 individual scan tiles at 100x magnification. We encountered two common types of montage-related artefacts: (1) duplicated data points along stitches, and (2) horizontal or vertical (x-y) shifts between adjacent tiles (Pilchak et al., 2011). Duplicated data points, usually limited to a strip of 1-2 pixels in width, are observed along edges of adjacent tiles in montaged maps. We eliminated duplicated data points at stitches by simply removing these repeated pixels using an automated algorithm (e.g., pointed by green arrows in Figs. 2(a), 3(a), 4(a)). Tile shifts appear as an x-y offset along grain boundaries in sample PIL271 (pointed by white arrows in Fig. 4(b)). Tile shifts are unlikely to cause significant errors in microstructural analyses because the x-y offsets are small (<100 μm) and noticeable only along the margins of tiles.

3 Results

3.1 Starting material

Undeformed coarse-grained ice samples exhibit a homogeneous microstructure with slightly irregular grain boundaries and a small number of intragranular boundaries (mostly low angle) (Figs. 1(a, g))— compared with fine-grained (~300 μm) ice samples fabricated via the same "flood-freeze" method (Fan et al., 2021, 2020). Grain sizes follow a slightly left-skewed log-linear distribution, with a peak at ~1300 μm, and a tail extending down to ~300 μm (Fig. 1(b)). Thus, although the "wet sieve" method (Sect. 2.1) is more effective (than the "dry sieve" method, e.g., Qi et al., 2017) for removing unwanted finer grains, our starting material contained a small (<10%) area fraction of grains with diameters <1.0 mm (Fig. 1(b)). Most grains are equant, with aspect ratios of all grains <4, and 80% of grains with aspect ratios <2 (Fig. 1(c)). Shape preferred orientation is weak, with a small rose diagram peak of grain long axes oriented at ~30° from the sample compression axis (Fig. 1(d)). The starting material has a near-random CPO (Figs. 1(e-f)). Intragranular boundaries and grain boundaries have misorientation axes with near-random crystallographic orientations, although there is a slight bias towards grain boundary misorientation axes lying within the basal plane (Fig. 1(h)).

3.2 Microstructure of deformed samples

3.2.1 Grain size statistics

All deformed samples are characterised by bigger grains surrounded by networks of smaller grains (Figs. 2(a-b), 3(a-b), 4(a-b)). All samples have similar arithmetic mean grain sizes, regardless of strain rate, much smaller than the average undeformed sample grain size (Table 1). Grain size histograms of deformed samples are bimodal: the first peak, at fine grain sizes (50–60 μm), is right-skewed, with a tail extending towards the second peak at 1000–2000 μm; the two grain size peaks are separated by a minimum at ~300 μm (Figs. 2(c), 3(c), 4(c)). Area-weighted grain size histograms reveal that although big (≥300 μm) grains are less numerous than small (<300 μm) grains, they occupy >75% of the mapped area in each deformed sample (Figs. 2(c), 3(c), 4(c)). Note that the small grain population (<300 μm) does not exist in the undeformed sample (Fig. 1(b)). To interrogate the microstructures of these two grain size populations, we herein refer to grains smaller than 300 μm as *small* grains, and grains larger than or equal to 300 μm as *big* grains. To identify these specific terms, they will be written in italics herein.

3.2.2 Grain populations

Deformed samples contain a significant number of "grains" (domains) with high aspect ratios (≥ 4) and relatively straight grain boundaries (Figs. 2(b, d), 3(b, d), 4(b, d)), which are not observed in the undeformed material (Fig. 1(c)). These high aspect ratio, straight-sided domains develop within the interiors of *big* grains, particularly near the tips of those grains (Figs. 2(a, b), 3(a, b), 4(a, b)). We identify these high aspect ratio grains as kink domains and separate them out for further analysis using an aspect ratio threshold of 4 (i.e., "grains" with aspect ratios ≥4 are treated as kink domains). The shape preferred orientation (SPO) of kink domains shows a significant maximum at ~90° from the compression axis; that is, kink domains' long axes tend to lie in the plane normal to the compression direction. The SPO of grains with relatively low aspect ratios (<4), on the other hand, is weaker (Figs. 2(e), 3(e), 4(e)). In deformed samples, grains with low aspect ratios have similar distributions of basal plane orientations (red histogram, Fig. 5(a)) as in the undeformed sample (black circles, Fig. 5(a)), as well as expected distribution of basal plane orientations for a random CPO (green curve, Fig. 5(a)). Kink domains, on the other hand, tend to have a greater proportion of basal planes oriented at low angles (0°-30°) to the compression direction (blue histogram, Fig. 5(a)).

In deformed samples, almost all the *big* grains with low aspect ratios (<4) contain intragranular boundaries—note that unless specified otherwise, "intragranular boundaries" herein refers to boundaries of all misorientation angles, both high and low. In contrast, the frequency of *small* grains containing intragranular boundaries is low, particularly for *small* grains with low aspect ratios (<4) (Table 1). Moreover, for grains with low aspect ratios, the grain orientation spread (GOS) value—an average of misorientation angle between each pixel in a grain and the mean orientation of that grain—is lower for *small* grains than *big* grains (Table 1). These observations suggest *small* low-aspect-ratio grains, which do not appear in the starting material (Fig. 1(c)), are less internally deformed and, thus, are likely to be nuclei produced by dynamic recrystallization (Bailey and Hirsch, 1962; Tullis and Yund, 1985). Accordingly, we herein refer to *small* grains with aspect ratios lower than 4 as recrystallized grains. *Big* grains with low aspect ratios (<4) are widely observed in the starting material (Figs. 1(a, c)) and are therefore referred as remnant grains. Recrystallized grains have a close-to-random grain boundary misorientation axes distribution, distinct from remnant grains and kink domains, which show primary maxima of boundary misorientation axes within the ice basal plane (Figs. 2(h), 3(h), 4(h)).

3.2.3 Intragranular boundary characteristics

For all deformed samples, intragranular boundaries comprise low-angle (< 10°) and high-angle (> 10°) components (Figs. 2(f), 3(f), 4(f)). High-angle intragranular boundaries are mostly straight or slightly curved. Similarly, low-angle intragranular boundaries are mostly straight or slightly curved, although a small number have strong curvature (Figs. 2(f, g), 3(f, g), 4(f, g)). Furthermore, intragranular boundaries usually intersect the boundary of their parent *big* grain on one side and terminate within their parent *big* grain on the other end; in other words, intragranular boundaries typically do not completely bisect their parent *big* grain (Figs. 2(f, g), 3(f, g), 4(f, g)).

Many (low- and high-angle) intragranular boundaries have misorientation axes lying within the basal plane, as indicated by a dominance of green-to-cyan-to-blue colours in boundary misorientation axis maps (Figs. 2(g), 3(g), 4(g)). Misorientation axes are plotted in contoured inverse pole figures (IPFs) (Figs. 2(h), 3(h), 4(h)). The distribution of low- or high-angle intragranular boundary misorientation axes does not change substantially with stress/strain rate. All the grain populations show similar distribution patterns between low- and high-angle intragranular boundaries—they are characterised by primary maxima within the basal plane (Figs. 2(h), 3(h), 4(h)). However, the intensity of maxima (as indicated by the maximum MUD value) is greater for high-angle intragranular boundaries than for low-angle intragranular boundaries (Figs. 2(h), 3(h), 4(h)).

3.2.4 Misorientation statistics and density of kink bands within remnant grains

We isolated the intragranular boundaries that have misorientation axes within 1° of the ice basal plane (i.e., kink band boundaries, Sect. 3.2.3) within remnant grains (Fig. 5(b)) to further quantify their misorientation statistics. For all deformed samples, the misorientation angle distribution of kink bands exhibit a unimodal distribution with a peak at the cut-off misorientation angle of 4° and a tail extending to misorientation angles up to 60–70° (grey bars in Fig. 5(b)). Most (>60%) kink bands have misorientation angles larger than 10°, a considerable proportion (>20%) of which has misorientation angles larger than 20° (red lines in Fig. 5(b)). On the contrary, kink bands within undeformed samples have misorientation angles mostly below 10° (pink lines in Fig. 5(b)).

For each remnant grain (≥300 µm, aspect ratio <4), we calculated the density of kink bands—i.e., the total length of kink bands per grain area—as a function of the angle between the mean grain basal plane orientation and the compression axis (Fig. 5(c)). In all deformed samples, remnant grains generally have higher kink band densities than undeformed samples (Fig. 5(c)). Furthermore, within deformed samples, kink band density gradually decreases as grain basal planes become more steeply inclined with respect to the compression axis; that is, grains with basal planes normal to the compression axis have the lowest kink band densities. This pattern is the same across experiments with different strain rates.

3.3 Crystallographic preferred orientation (CPO)

For each sample, we calculated the CPO of all grains, remnant grains, recrystallized grains, and kink domains (Fig. 6(a)), using both the orientations of all pixels and the mean orientation of each grain. Here we discuss the CPOs calculated from all pixels, for simplicity, although the mean-orientation CPOs are very similar (Sect. S1 of the supplement). CPO intensity is calculated using the M-index (Skemer et al., 2005). The *c*-axis CPOs (pole figures) are summarized in Fig. 6(b).

3.3.1 All grains and remnant grains

Pole figures for all grains and remnant grains are very similar, both characterised by three to four *c*-axes maxima lying within a weak, poorly defined open cone (small circle) or possibly cluster centred around the compression axis. The *a*-axes and poles to the *m*-plane lie within a broad, poorly defined girdle normal to the compression axis.

3.3.2 Kink domains

Kink domains exhibit the strongest CPO of the different grain populations, as indicated by the relatively high M-index values (Fig. 6(a)). The *c*-axes of kink domains generally lie near the plane normal to the compression axis (Figs. 6(a, b)). The *a*-axes and poles to the *m*-plane define a weak, narrow cone or cluster centred around the compression axis (Fig. 6(a)).

3.3.3 Recrystallized grains

Recrystallized grains have the weakest CPOs of different grain populations (see M-index and MUD values; Fig. 6(a)). Their *c*-axes define a weak, broad maximum, lying within the plane containing the compression axis, but centred around an axis inclined ~45° from the compression axis. Although the deformation (uniaxial compression) geometry has axial symmetry around the compression axis, the *c*-axis pole figures are not axially symmetric (Fig. 6(b)). The *a*-axes and poles to the *m*-plane have a near-random distribution.

4 Discussion

4.1 Microstructural development

4.1.1 Nucleation

Subgrain rotation recrystallization

In all deformed samples, "core-and-mantle" structures (White, 1976)—i.e., networks of *small,* recrystallized grains encircling remnant, *big* grains—are well developed (Figs. 2(b), 3(b), 4(b)). Moreover, equiaxed-shaped subgrains defined by curved intragranular boundaries intersecting with grain boundaries of the host remnant grains are widely observed within deformed samples (pointed by black arrows in Figs. 2(f), 3(f), 4(f)). Core-and-mantle structures and subgrains along the margins of remnant grains are typical of subgrain rotation recrystallization (Halfpenny et al., 2006; Poirier and Nicolas, 1975; Urai et al., 1986). Nevertheless, we note that some recrystallized grains may have formed via bulging nucleation (Halfpenny et al., 2006) and/or "spontaneous" nucleation (Hasegawa and Fukutomi, 2002).

Grain segmentation via kinking

Kink domains, encompassed by high-angle boundaries, are widely developed within all deformed samples (Sect. 3.2.2). Thus, in addition to grain nucleation by subgrain rotation recrystallization, new (high angle) grain boundary area is also formed via kinking, which leads to further grain segmentation and grain size reduction. In other words, kinking also acts as a grain nucleation mechanism, forming new high-aspect-ratio grains (kink bands) at the expense of remnant grains.

4.1.2 Kink bands characteristics

Straight or slightly curved intragranular boundaries are widely observed (Figs. 2(f), 3(f), 4(f)), the low- and high-angle components of which have very similar misorientation axis distributions with maxima lie predominantly within the basal plane (Figs. 2(g, i), 3(g, i), 4(g, i)), matching kink band observations from previous studies (Piazolo et al., 2015; Seidemann et al., 2020). Most (~60%) kink bands have misorientation angles higher than 5-10°, which is commonly used to distinguish subgrain boundaries from grain boundaries in ice (Fan et al., 2020; Qi et al., 2017), and a considerable proportion (>20%) of kink bands has misorientation angles higher than 20° (Fig. 5(b)). Therefore, although kink bands can become highly misoriented with respect to their parent grain, kink bands remain strongly crystallographically controlled—with rational misorientation axes lying within the basal plane, in this case.

Misorientation statistics of kink bands can help us to better understand subgrain rotation, because kinking and subgrain rotation have very similar kinematics—they both involve a continuous crystal lattice bending due to the progressive addition of dislocations to kink or subgrain walls (Bell et al., 1986; Poirier and Nicolas, 1975; Urai et al., 1986). Our data show that frequency of kink bands decreases continuously from low (4°) to high (60-70°) misorientation angles (Fig. 5(b)), suggesting that kinking more likely results from continuous lattice bending, rather than an instantaneous lattice bending that would lead to the immediate formation of high-angle kink bands. Therefore, we suggest that the subgrain rotation process can likewise proceed to high misorientation angles (>20°), and that (sub)grain boundaries should remain crystallographically controlled throughout their rotation. Such phenomena have been observed in metals, high angle tilt walls, for example, in single crystals (or coarse-grained samples) has been used to measure boundary energy and mobilities (Humphreys et al., 2017). Thus, the nature of recrystallized grains with grain boundaries lacking crystallographic control (with a close-to-random grain boundary misorientation axes distribution) (Sect. 3.2.2) may need to be reappraised. A common model is that low angle dislocation arrays (subgrain walls) break down above a certain misorientation angle as the boundary cannot maintain a dislocation structure to higher angles—in other words, there is a limit of misorientations that can be sustained by arrays of dislocations (Read-Shockely equation: Humphreys et al., 2017; Read and Shockley, 1950). So maybe the key process required for the boundary misorientation axis to change is the formation of grain boundaries resulting from the connection of high-angle intragranular boundaries. The enclosure of grain boundaries allows other processes such as grain boundary sliding and grain boundary migration to proceed, and these processes require the boundary structure to change (Duval, 1985; Hondoh and Higashi, 1983; Ree, 1994).

4.2 Crystallographic controls and effects of kinking

Remnant grain *c*-axis pole figures show multiple maxima, arranged in a weak cluster or open cone centred around the compression axis (Fig. 6(a)). Multiple-maxima ice *c*-axis fabrics arise when the number of grains measured from a single sample plane is not sufficient for a fully representative CPO (Monz et al., 2021). Cone and cluster CPOs are commonly observed in ice samples deformed under uniaxial compression conditions, and are thought to arise from varying contributions of strain-induced grain boundary migration (GBM) and grain rotation due to dislocation glide (Kamb, 1972; Vaughan et al., 2017).

Recrystallized grains have a CPO that is much weaker than the other grain populations (Sect. 3.3.3). Weak recrystallized grain CPOs have been reported in previous studies on experimentally deformed ice (Fan et al., 2020) as well as naturally and experimentally deformed rock (Bestmann and Prior, 2003). Published models that attempt to explain CPO weakening of recrystallized grains include grains boundary sliding (Warren and Hirth, 2006), bulging nucleation (Falus et al., 2011) and nucleation with random orientations (Hasegawa and Fukutomi, 2002).

Kink domains exhibit a *c*-axis girdle within the plane normal to the compression axis, forming a CPO that is distinct from remnant and recrystallized grains (Fig. 6). Nevertheless, at ~10% strain in this study, the CPO of all grains (bulk CPO) is similar to the CPO of remnant grains alone, suggesting kink domains have a weak influence on the bulk CPO at low strains. Further studies should be conducted to investigate the influence of kink domains in the modification of bulk CPO at high strains.

4.2.1 Grain orientation controls on kinking activity

Previous studies suggest that materials with strong mechanical anisotropy, like ice-1h, are prone to kinking (Piazolo et al., 2015; Seidemann et al., 2020). Furthermore, deformation experiments on layered metals or geological materials (e.g., graphite, mica) show that kinks predominately form when basal planes are oriented poorly for easy slip (see review by Barsoum, 2020). Thus, we might expect to see high kink band densities in host grains with basal planes oriented sub-parallel and sub-perpendicular to the compression axis (i.e., in grains with hard, low-basal-Schmid-factor orientations). However, while we find that kink band density is highest within remnant grains with basal planes oriented sub-parallel to the compression axis, there is almost a complete absence of kink bands within host grains that have basal planes oriented sub-perpendicular to the compression axis (Sect. 3.2.4; Fig. 5(a)). In other words, the activity of kinking does not simply correlate with basal Schmid factor, as suggested by previous kinking studies and models.

4.2.2 Modelling crystallographic controls on kink nucleation

To examine grain orientation controls on kinking activities in further detail, we employ a 2-D kink nucleation model developed by Honea and Johnson (1976) and Nishikawa and Takeshita (1999). The model proposes that under uniaxial compression, the critical shear stress, σ_s, required for a kink band to accommodate deformation is as follows:

$$\sigma_s = \frac{\sigma_1}{cos^2\theta + \frac{sin\theta cos\theta}{tan\ \varphi}}, \tag{1}$$

where σ_1 is the maximum principal stress (i.e., stress along the compression axis in this case), φ is the misorientation angle between the basal plane of the kink band and the basal plane of its host lattice, and θ is the angle between the basal plane of the host lattice and the compression axis (Fig. 7(a)). Equation (1) implies that, for a host lattice (e.g., blue lines in Fig. 7(a)) containing one or more kink bands (e.g., red lines in Fig. 7(a)), the critical shear stress, σ_s, required for the kink bands to continue deforming depends on (1) the relative magnitudes of the stresses resolved on the basal planes of kink bands and the basal planes of the host lattice, and (2) the relative orientation between the compression axis and the basal plane of the host lattice.

The model makes two predictions for polycrystalline aggregates deforming solely via kinking. First, that the critical shear stress required for a kink band to accommodate deformation, σ_s, increases as a kink band becomes more misoriented (increasing φ) with respect to its host grain. That is, it becomes harder for kink bands to develop as they become more misoriented with respect to their host grain. Second, the model predicts that for small kink-host misorientation angles (i.e., low φ—cool coloured curves in Fig. 7(b)), kink band density should be greatest. This is because σ_s will be lowest in host grains with basal planes oblique (θ=30-50°) to the compression axis (Fig. 7(b)). For large kink-host misorientation angles (i.e., high φ—hot coloured curves in Fig. 7(b)), kink band density should be greatest. This is because σ_s will be lowest in host grains with basal planes sub-parallel (θ=0-20°) to the compression axis (Fig. 7(b)).

However, our experimental observations do not match the second model prediction. For kink boundary misorientation angles, φ, smaller than 20°—as are common in our samples (Fig. 5(b))—kink band densities should be greatest within remnant grains that have basal planes oblique to the compression axis (θ=30-50°; Fig. 7(b)). In contrast, we find that remnant grains with basal planes parallel to the compression axis have the highest densities of intragranular boundaries, while remnant grains with basal planes normal to the compression axis have the lowest densities of intragranular boundaries (Fig. 5(b), Sect. 3.2.4). One way to rationalise the mismatch between the experimental observations and model predictions is that, in our samples, both kinking and dynamic recrystallization processes (e.g., strain-induced grain boundary migration, subgrain rotation recrystallization and dynamic recovery) are active, whereas the model addresses deformation via kinking alone. Kink band densities (Fig. 5(b)) do not obey the trend predicted by Eq. (1) (Fig. 7(b)) because the balance between recovery, recrystallization, and kinking, is different for grains in different crystallographic orientations, and evolves as those grains undergo deformation. Figure 7(c) schematically illustrates the relationship between ice *c*-axes/basal plane orientations and activities of kinking and dynamic recrystallization processes. Grains with basal planes oblique to the compression axis (θ=30-50°; e.g., the green grain, G3, in Fig. 7(c)) are optimally oriented for both kinking and easy slip, i.e., dislocation glide on the ice basal plane. Previous studies suggest that intragranular strain incompatibilities can be efficiently relaxed through the selective growth of grains in easy slip orientations, at the expense of grains in hard slip orientations, via strain-induced grain boundary migration (GBM) (Fig. 7(d); Derby and Ashby, 1987; Humphreys et al., 2017; Vaughan et al., 2017). Therefore, kinking may be less important within grains in easy slip orientations (i.e., with basal planes oblique to the compression axis here). Grain with basal planes sub-parallel to shortening ($\theta \approx 0°$; e.g., the blue grain, G2, in Fig. 7(c)), on the other hand, are unfavourably oriented for basal dislocation glide; thus, strain-induced GBM is inhibited, and intragranular strain incompatibilities must be accommodated predominately by kinking (Fig. 7(d)). For grains with basal planes sub-perpendicular to shortening ($\theta \approx 90°$; e.g., the red grain, G1, in Fig. 7(c)), the critical shear stress, σ_s, required for the progression of kinking exceeds the maximum principal stress, σ_1, except perhaps at very small kink-host misorientation angles, $\varphi < 10°$ (Fig. 7(b)). Thus, grains with basal planes sub-perpendicular to the compression axis are fundamentally stable and difficult to kink (Fig. 7(d)), consistent with our microstructural data showing that grains in these orientations have the lowest density of kink bands (Fig. 5(b)). Grains with basal planes oriented normal to the compression axis are stronger than grains with basal planes oriented parallel to the compression axis—the latter kink while the former do not—even though they are equally poorly oriented for basal dislocation glide. Strain in the hardest ($\theta \approx 90°$) grains might therefore be accommodated by non-basal dislocation glide (e.g., Chauve et al., 2017).

4.3 Implications for planetary ice sheets

In terrestrial glacial settings, kink bands have only been observed within folded ice layers, where local stresses and strain rates are relatively high (Jansen et al., 2016). Thus, kinking is unlikely to have a widespread control on the mechanics of terrestrial polar ice flow. However, for other planetary bodies, where the deformation of ice sheets is often subject to large stresses and low temperatures (see review by Journaux et al., 2020), kinking might be important in controlling ice deformation mechanics. Our experimental data imply that under large stresses, kinking plays a key role in segmenting new grains from original grains (nucleation) (Sect. 4.1.1) and accommodating large plastic strain when thermally activated creep processes (e.g., vacancy diffusion and dislocation climb) are inefficient (Sect. 4.2), as is likely the case in the cold outer solar system.

5 Summary

1. Microstructural analyses were conducted on coarse-grained ice (~1300 μm) deformed under relatively high uniaxial stresses (>5 MPa). Within deformed samples, kink domains (i.e., high-aspect-ratio (≥ 4) grains) are widely developed. Recrystallized (small, low-aspect-ratio) grains also form via nucleation, which is facilitated by subgrain rotation recrystallization, further contributing to grain size reduction. Thus, subgrain rotation and kinking both contribute to grain segmentation and grain size reduction.

2. Kink bands are composed of both low- (<10°) and high-angle (mostly 10–20°, many >20°) components. Kink bands (of both low and high misorientation angles) have misorientation axes lying predominately within the ice basal plane. Previous studies suggest the kinematics of kinking and subgrain rotation are fundamentally the same. Together, these observations suggest that kinking and subgrain rotation can evolve to moderately large misorientation angles, but remain crystallographically controlled, i.e., they are unlikely, by themselves, to change the misorientation axis.

3. Kink domains are preferentially oriented with *c*-axes sub-perpendicular to the compression axis, unlike remnant grains that have weak cluster and narrow cone-shaped *c*-axis distributions centred around the compression axis, and nucleated grains that have near-random *c*-axis distributions. Bulk crystallographic fabrics most closely resemble the CPO of remnant grains, suggesting that kinking does not significantly modify bulk CPOs, at low strains.

4. Kink band densities decrease monotonically as a function of the angle between the host grain basal plane and the compression axis. Kink domains are nearly absent in grains with basal planes sub-perpendicular to the compression axis, consistent with kink models showing that grains with easy-slip planes (i.e., basal planes, in this case) sub-perpendicular to shortening are fundamentally stable and uneasy to kink since the critical shear stress required for kinking exceeds the applied stress. Grains with basal planes sub-parallel to shortening, on the other hand, have the highest kink band densities. This observation is not expected from models that solely consider strain accommodation via kinking—instead, models suggests that grains with basal planes sub-parallel to shortening should be harder to kink than grains with basal planes oblique to shortening. We propose that the inconsistency between kink model predictions and experimental observations may be reconciled by considering the activity of both kinking and dynamic recrystallization during deformation. For grains with basal planes oblique to compression, (i.e., in easy basal slip orientations), strain-induced grain boundary migration (GBM) might be sufficient to relax the intragranular strain incompatibility and kinking is thus less important. For grains with basal planes sub-parallel to compression (i.e., in hard-slip orientations), strain-induced GBM should be inhibited. Consequently, large intragranular strain incompatibilities can be relaxed via kinking, when other processes, such as subgrain rotation recrystallization, are not efficient enough under large uniaxial stresses.

Data availability

Data will be available via Mendeley Data (open-access data share run by Elsevier with a permanent doi) once the manuscript is accepted.

Competing interests

The authors declare that they have no conflict of interest.

Acknowledgements

We are thankful to Pat Langhorne for providing the cold-room facility at University of Otago. This work was supported by a NASA fund (grant no. NNX15AM69G) to David L. Goldsby and two Marsden Funds of the Royal Society of New Zealand (grant nos. UOO1116, UOO052) to David J. Prior. Sheng Fan was supported by the University of Otago doctoral scholarship, the Antarctica New Zealand doctoral scholarship and two New Zealand Antarctic Research Institute (NZARI) Early Career Researcher Seed Grants.

References

Bachmann, F., Hielscher, R., Schaeben, H., 2011. Grain detection from 2d and 3d EBSD data—Specification of the MTEX algorithm. Ultramicroscopy 111, 1720–1733. https://doi.org/10.1016/j.ultramic.2011.08.002

Bailey, J.E., Hirsch, P.B., 1962. The recrystallization process in some polycrystalline metals. Proc. R. Soc. London. Ser. A. Math. Phys. Sci. 267, 11–30. https://doi.org/10.1098/rspa.1962.0080

Barsoum, M.W., 2020. Ripplocations: A Progress Report. Front. Mater. 7, 1–17. https://doi.org/10.3389/fmats.2020.00146

Bell, I.A., Wilson, C.J.L., McLaren, A.C., Etheridge, M.A., 1986. Kinks in mica: Role of dislocations and (001) cleavage. Tectonophysics 127, 49–65. https://doi.org/10.1016/0040-1951(86)90078-8

Bestmann, M., Prior, D.J., 2003. Intragranular dynamic recrystallization in naturally deformed calcite marble: Diffusion accommodated grain boundary sliding as a result of subgrain rotation recrystallization. J. Struct. Geol. 25, 1597–1613. https://doi.org/10.1016/S0191-8141(03)00006-3

Chauve, T., Montagnat, M., Piazolo, S., Journaux, B., Wheeler, J., Barou, F., Mainprice, D., Tommasi, A., 2017. Non-basal dislocations should be accounted for in simulating ice mass flow. Earth Planet. Sci. Lett. 473, 247–255.

Cole, D.M., 1979. Preparation of polycrystalline ice specimens for laboratory experiments. Cold Reg. Sci. Technol. 1, 153–159. https://doi.org/10.1016/0165-232X(79)90007-7

Derby, B., Ashby, M.F.F., 1987. On dynamic recrystallisation. Scr. Metall. 21, 879–884. https://doi.org/10.1016/0036-9748(87)90341-3

Drury, M.R., Pennock, G.M., 2007. Subgrain Rotation Recrystallization in Minerals. Mater. Sci. Forum 550, 95–104. https://doi.org/10.4028/www.scientific.net/msf.550.95

Durham, W., Stern, L., 2001. Rheological Properties of Water Ice—Applications to Satellites of the Outer Planets. Annu. Rev. Earth Planet. Sci. 29, 295–330. https://doi.org/10.1146/annurev.earth.29.1.295

Duval, P., 1985. Grain growth and mechanical behaviour of polar ice. Ann. Glaciol. 6, 79–82. https://doi.org/10.1017/s0260305500010041

Duval, P., 1979. Creep and recrystallization of polycrystalline ice. Bull. Minéralogie 102, 80–85. https://doi.org/10.3406/bulmi.1979.7258

Duval, P., Ashby, M.F., Anderman, I., 1983. Rate-controlling processes in the creep of polycrystalline ice. J. Phys. Chem. 87, 4066–4074. https://doi.org/10.1021/j100244a014

Falus, G., Tommasi, A., Soustelle, V., 2011. The effect of dynamic recrystallization on olivine crystal preferred orientations in mantle xenoliths deformed under varied stress conditions. J. Struct. Geol. 33, 1528–1540.

Fan, S., Hager, T.F., Prior, D.J., Cross, A.J., Goldsby, D.L., Qi, C., Negrini, M., Wheeler, J., 2020. Temperature and strain controls on ice deformation mechanisms: insights from the microstructures of samples deformed to progressively higher strains at −10, −20 and −30 °C. Cryosph. 14, 3875–3905. https://doi.org/10.5194/tc-14-3875-2020

Fan, S., Prior, D.J., Cross, A.J., Goldsby, D.L., Hager, T.F., Negrini, M., Qi, C., 2021. Using grain boundary irregularity to quantify dynamic recrystallization in ice. Acta Mater. 209, 116810. https://doi.org/10.1016/j.actamat.2021.116810

Gay, N.C., Weiss, L.E., 1974. The relationship between principal stress directions and the geometry of kinks in foliated rocks. Tectonophysics 21, 287–300. https://doi.org/10.1016/0040-1951(74)90056-0

Halfpenny, A., Prior, D.J., Wheeler, J., 2006. Analysis of dynamic recrystallization and nucleation in a quartzite mylonite. Tectonophysics 427, 3–14. https://doi.org/10.1016/j.tecto.2006.05.016

Hasegawa, M., Fukutomi, H., 2002. Microstructural Study on Dynamic Recrystallization and Texture Formation in Pure Nickel. Mater. Trans. 43, 1183–1190.

Heard, H.C., Durham, W.B., Boro, C.O., Kirby, S.H., 1990. A triaxial deformation apparatus for service at 77 ≤ T ≤ 273 K, in: The Brittle-Ductile Transition in Rocks. pp. 225–228. https://doi.org/10.1029/GM056p0225

Hidas, K., Tommasi, A., Mainprice, D., Chauve, T., Barou, F., Montagnat, M., 2017. Microstructural evolution during thermal annealing of ice-I h. J. Struct. Geol. 99, 31–44. https://doi.org/10.1016/j.jsg.2017.05.001

Hondoh, T., Higashi, A., 1983. Generation and absorption of dislocations at large-angle grain boundaries in deformed ice crystals. J. Phys. Chem. 87, 4044–4050. https://doi.org/10.1021/j100244a009

Honea, E., Johnson, A.M., 1976. A theory of concentric, kink and sinusoidal folding and of monoclinal flexuring of compressible, elastic multilayers: IV. Development of sinusoidal and kink folds in multilayers confined by rigid boundaries. Tectonophysics 30, 197–239. https://doi.org/10.1016/0040-1951(76)90187-6

Humphreys, F.J., Hatherly, M., Rollett, A., 2017. Recrystallization and Related Annealing Phenomena, Third. ed. Elsevier Ltd.

Jansen, D., Llorens, M.G., Westhoff, J., Steinbach, F., Kipfstuhl, S., Bons, P.D., Griera, A., Weikusat, I., 2016. Small-scale disturbances in the stratigraphy of the NEEM ice core: Observations and numerical model simulations. Cryosphere 10, 359–370. https://doi.org/10.5194/tc-10-359-2016

Journaux, B., Kalousová, K., Sotin, C., Tobie, G., Vance, S., Saur, J., Bollengier, O., Noack, L., Rückriemen-Bez, T., Van Hoolst, T., Soderlund, K.M., Brown, J.M., 2020. Large Ocean Worlds with High-Pressure Ices. Space Sci. Rev. 216. https://doi.org/10.1007/s11214-019-0633-7

Kamb, B., 1972. Experimental Recrystallization of Ice Under Stress, in: Flow and Fracture of Rocks. American Geophysical Union, pp. 211–241. https://doi.org/10.1029/GM016p0211

Means, W.D., 1983. Microstructure and micromotion in recrystallization flow of octachloropropane: A first look. Geol. Rundschau 72, 511–528. https://doi.org/10.1007/BF01822080

Monz, M.E., Hudleston, P.J., Prior, D.J., Michels, Z., Fan, S., Negrini, M., Langhorne, P.J., Qi, C., 2021. Full crystallographic orientation (c and a axes) of warm, coarse-grained ice in a shear-dominated setting: a case study, Storglaciären, Sweden. Cryosph. 15, 303–324. https://doi.org/10.5194/tc-15-303-2021

Nishikawa, O., Takeshita, T., 1999. Dynamic analysis and two types of kink bands in quartz veins deformed under subgreenschist conditions. Tectonophysics 301, 21–34. https://doi.org/10.1016/S0040-1951(98)00219-4

Piazolo, S., Montagnat, M., Grennerat, F., Moulinec, H., Wheeler, J., 2015. Effect of local stress heterogeneities on dislocation fields: Examples from transient creep in polycrystalline ice. Acta Mater. 90, 303–309. https://doi.org/10.1016/j.actamat.2015.02.046

Pilchak, A.L., Shiveley, A.R., Tiley, J.S., Ballard, D.L., 2011. AnyStitch: A tool for combining electron backscatter diffraction data sets. J. Microsc. 244, 38–44. https://doi.org/10.1111/j.1365-2818.2011.03496.x

Poirier, J.-P., Guillopé, M., 1979. Deformation induced recrystallization of minerals. Bull. Minéralogie 102, 67–74. https://doi.org/10.3406/bulmi.1979.7256

Poirier, J.P., Nicolas, A., 1975. Deformation-Induced Recrystallization Due to Progressive Misorientation of Subgrains, with Special Reference to Mantle Peridotites. J. Geol. 83, 707–720. https://doi.org/10.1086/628163

Prior, D.J., 1999. Problems in determining the misorientation axes, for small angular misorientations, using electron backscatter diffraction in the SEM. J. Microsc. 195, 217–225. https://doi.org/10.1046/j.1365-2818.1999.00572.x

Prior, D.J., Lilly, K., Seidemann, M., Vaughan, M., Becroft, L., Easingwood, R., Diebold, S., Obbard, R., Daghlian, C., Baker, I., Caswell, T., GOLDING, N., GOLDSBY, D., DURHAM, W.B., PIAZOLO, S., WILSON, C.J.L., 2015. Making EBSD on water ice routine. J. Microsc. 259, 237–256. https://doi.org/10.1111/jmi.12258

Qi, C., Goldsby, D.L., Prior, D.J., 2017. The down-stress transition from cluster to cone fabrics in experimentally deformed ice. Earth Planet. Sci. Lett. 471, 136–147. https://doi.org/10.1016/j.epsl.2017.05.008

Read, W.T., Shockley, W., 1950. Dislocation Models of Crystal Grain Boundaries. Phys. Rev. 78, 275–289. https://doi.org/10.1103/PhysRev.78.275

Ree, J.H., 1994. Grain boundary sliding and development of grain boundary openings in experimentally deformed octachloropropane. J. Struct. Geol. 16, 403–418. https://doi.org/10.1016/0191-8141(94)90044-2

Seidemann, M., Prior, D.J., Golding, N., Durham, W.B., Lilly, K., Vaughan, M.J., 2020. The role of kink boundaries in the deformation and recrystallisation of polycrystalline ice. J. Struct. Geol. 136, 104010. https://doi.org/10.1016/j.jsg.2020.104010

Skemer, P., Katayama, I., Jiang, Z., Karato, S.I., 2005. The misorientation index: Development of a new method for calculating the strength of lattice-preferred orientation. Tectonophysics 411, 157–167. https://doi.org/10.1016/j.tecto.2005.08.023

Tullis, J., Yund, R.A., 1985. Dynamic recrystallization of feldspar: A mechanism for ductile shear zone formation. Geology 13, 238. https://doi.org/10.1130/0091-7613(1985)13<238:DROFAM>2.0.CO;2

Urai, J.L., Means, W.D., Lister, G.S., 1986. Dynamic recrystallization of minerals, in: Mineral and Rock Deformation: Laboratory Studies. pp. 161–199. https://doi.org/10.1029/GM036p0161

Vaughan, M.J., Prior, D.J., Jefferd, M., Brantut, N., Mitchell, T.M., Seidemann, M., 2017. Insights into anisotropy development and weakening of ice from in situ P wave velocity monitoring during laboratory creep. J. Geophys. Res. Solid Earth 122, 7076–7089. https://doi.org/10.1002/2017JB013964

Vernon, R.H., 2018. A Practical Guide to Rock Microstructure, 2nd ed. Cambridge University Press. https://doi.org/10.1017/9781108654609

Warren, J.M., Hirth, G., 2006. Grain size sensitive deformation mechanisms in naturally deformed peridotites. Earth Planet. Sci. Lett. 248, 438–450. https://doi.org/10.1016/j.epsl.2006.06.006

Weertman, J., 1983. Creep Deformation of Ice. Annu. Rev. Earth Planet. Sci. 11, 215–240. https://doi.org/10.1146/annurev.ea.11.050183.001243

Weikusat, I., Kuiper, E.-J.N., Pennock, G.M., Kipfstuhl, S., Drury, M.R., 2017. EBSD analysis of subgrain boundaries and dislocation slip systems in Antarctic and Greenland ice. Solid Earth 8, 883–898.

White, S., 1976. The Effects of Strain on the Microstructures, Fabrics, and Deformation Mechanisms in Quartzites. Philos. Trans. R. Soc. A Math. Phys. Sci. 283, 69–86.

Table 1. Summary of mechanical and microstructural data

<table>
<tr><th rowspan="2">Sample No.</th><th rowspan="2">Uniaxial true strain rate at the end of experiment, ~10% strain (s^{-1})</th><th rowspan="2">Uniaxial stress at the end of experiment, ~10% strain (MPa)</th><th rowspan="2">Grain size metrics (µm):
Lower quartile/
Median/
Higher quartile</th><th colspan="3">Within each grain population:
Total number of grains /
% grains contain low-angle (4°–10°) boundaries/
% grains contain low-angle (>10°) boundaries</th><th colspan="3">Metrics of GOS values (°) within each grain population:
Lower quartile/
Median/
Higher quartile</th></tr>
<tr></tr>
<tr><td rowspan="2">Undeformed</td><td rowspan="2">N/A</td><td rowspan="2">N/A</td><td rowspan="2">768/
1293/
1781</td><td colspan="3">All</td><td colspan="3">All</td></tr>
<tr><td colspan="3">173/
82%/
21%</td><td colspan="3">0.36/
0.45/
0.87</td></tr>
<tr><td colspan="4"></td><td>*Small, low-aspect-ratio (recrystallized grains)</td><td>*Big, low-aspect-ratio (remnant grains)</td><td>*High-aspect-ratio (kink domains)</td><td>*Small, low-aspect-ratio (recrystallized grains)</td><td>*Big, low-aspect-ratio (remnant grains)</td><td>*High-aspect-ratio (kink domains)</td></tr>
<tr><td>PIL275</td><td>1.2E-5</td><td>5.13</td><td>37/
51/
74</td><td>11107/
37%/
10%</td><td>321/
100%/
98%</td><td>1055/
65%/
26%</td><td>0.59/
0.98/
2.30</td><td>4.59/
6.47/
9.06</td><td>1.69/
2.95/
4.72</td></tr>
<tr><td>PIL270</td><td>3.0E-5</td><td>5.91</td><td>45/
62/
91</td><td>4047/
44%/
14%</td><td>239/
100%/
97%</td><td>704/
70%/
29%</td><td>0.65/
1.32/
3.01</td><td>4.81/
6.37/
8.53</td><td>1.92/
3.28/
5.19</td></tr>
<tr><td>PIL271</td><td>6.0E-5</td><td>6.67</td><td>37/
48/
64</td><td>9165/
26%/
7%</td><td>224/
100%/
98%</td><td>1022/
68%/
26%</td><td>0.41/
0.56/
1.44</td><td>4.23/
6.25/
8.99</td><td>1.91/
3.21/
4.83</td></tr>
</table>

* Small grains: grain size < 300 µm; big grains: grain size ≥ 300 µm. Low aspect ratio: aspect ratio < 4; high-aspect ratio: aspect ratio ≥ 4.

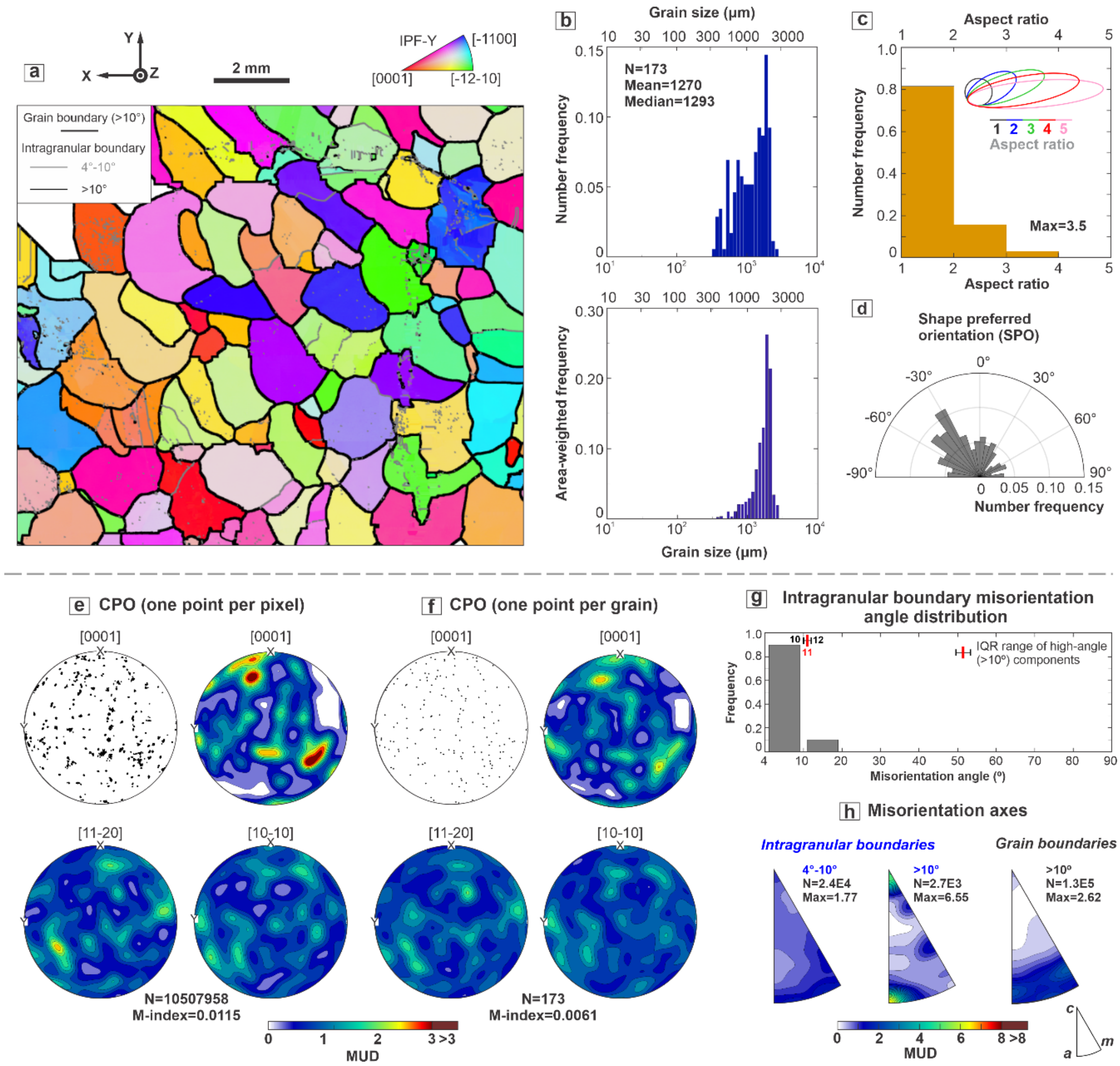

Figure 1. Microstructural analyses of undeformed coarse-grained ice. The EBSD data collected with 5 μm step size are presented as **(a)** orientation map coloured by IPF-Y, which uses the colour map to indicate the crystallographic axes that are parallel to the y-axis as shown by the black arrows. Grain boundaries are black. Intragranular boundaries are grey. We only show selected areas of EBSD maps so that the reader can resolve microstructural features. **(b)** Grain size statistics presented as grain size as a function of number frequency (**upper box**) or area-weighted frequency (**lower box**), with the grain size in logarithmic scale. **(c)** Distribution of aspect ratio. The max aspect ratio is marked within the box. Illustrative ellipses of different aspect ratios are also presented in the box. **(d)** Distribution of grain shape preferred orientation presented as rose diagram for all grains. CPOs for [0001] (*c*-axes), [11-20] *a*-axes and [10-10] (pole to the *m*-plane) are plotted on the basis of **(e)** one point per pixel and **(f)** one point per grain. Contoured CPOs are coloured by multiples of a uniform distribution (MUD). **(g)** Distribution of misorientation angle for intragranular boundaries. **(h)** Distribution of misorientation axes for intragranular boundaries and grain boundaries (>10°) displayed as contoured inverse pole figures (IPFs) with crystal reference frame.

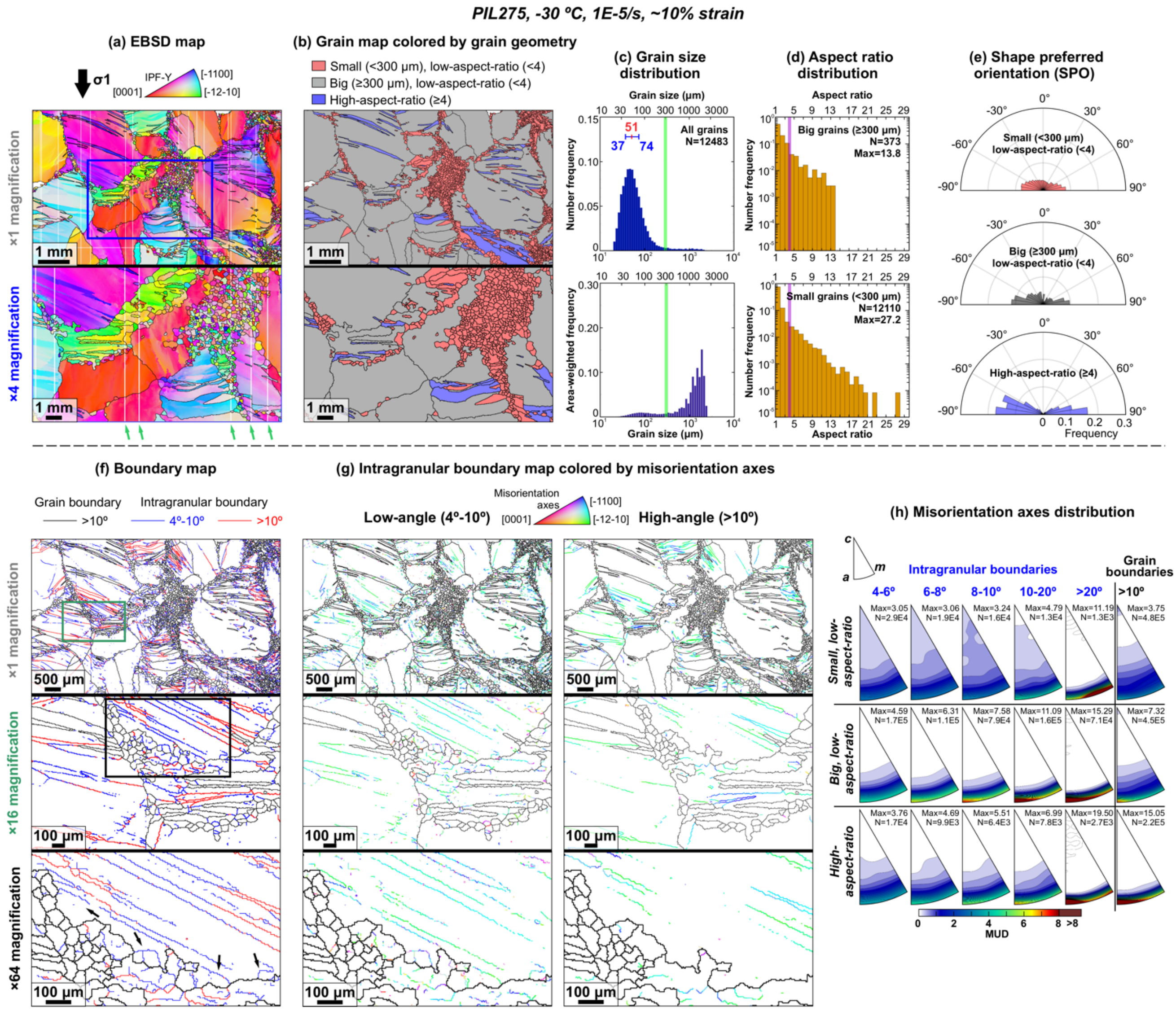

Figure 2. Microstructural analyses of sample PIL275. **(a)** A sub-area of the orientation map. Orientation map is coloured by IPF-Y, which uses the colour map to indicate the crystallographic axes that are parallel to the vertical shortening direction as shown by the black arrow. Grain boundaries (>10°) are shown black. **(b)** Grain map for grain populations with different sizes and shapes. **(c)** Grain size statistics presented as grain size as a function of number frequency (**upper box**) or area-weighted frequency (**lower box**), with the grain size in logarithmic scale. Interquartile range (IQR) of grain size is presented above the number-weighted grain size histogram. Median grain size is marked with red line, lower quartile and higher quartile grain sizes are marked with blue whiskers. **(d)** Distribution of aspect ratio for *big* (≥ 300 μm) and *small* (< 300 μm) grains, with the y-axis (number frequency) in logarithmic scale. **(e)** Distribution of grain shape preferred orientation presented as rose diagrams for different grain populations. Colour scheme is the same as **(b)**. Radial dimension of bars corresponds to frequency with the scale shown on the horizontal axis. **(f)** Boundary map. Black arrows indicate the intragranular boundary structures along grain boundaries. **(g)** Intragranular boundary maps coloured on the basis of misorientation axes. Misorientation axes are coloured by IPF colour code in crystal reference frame. **(h)** Distribution of misorientation axes in contoured inverse pole figures (IPFs) with crystal reference frame for different grain populations.

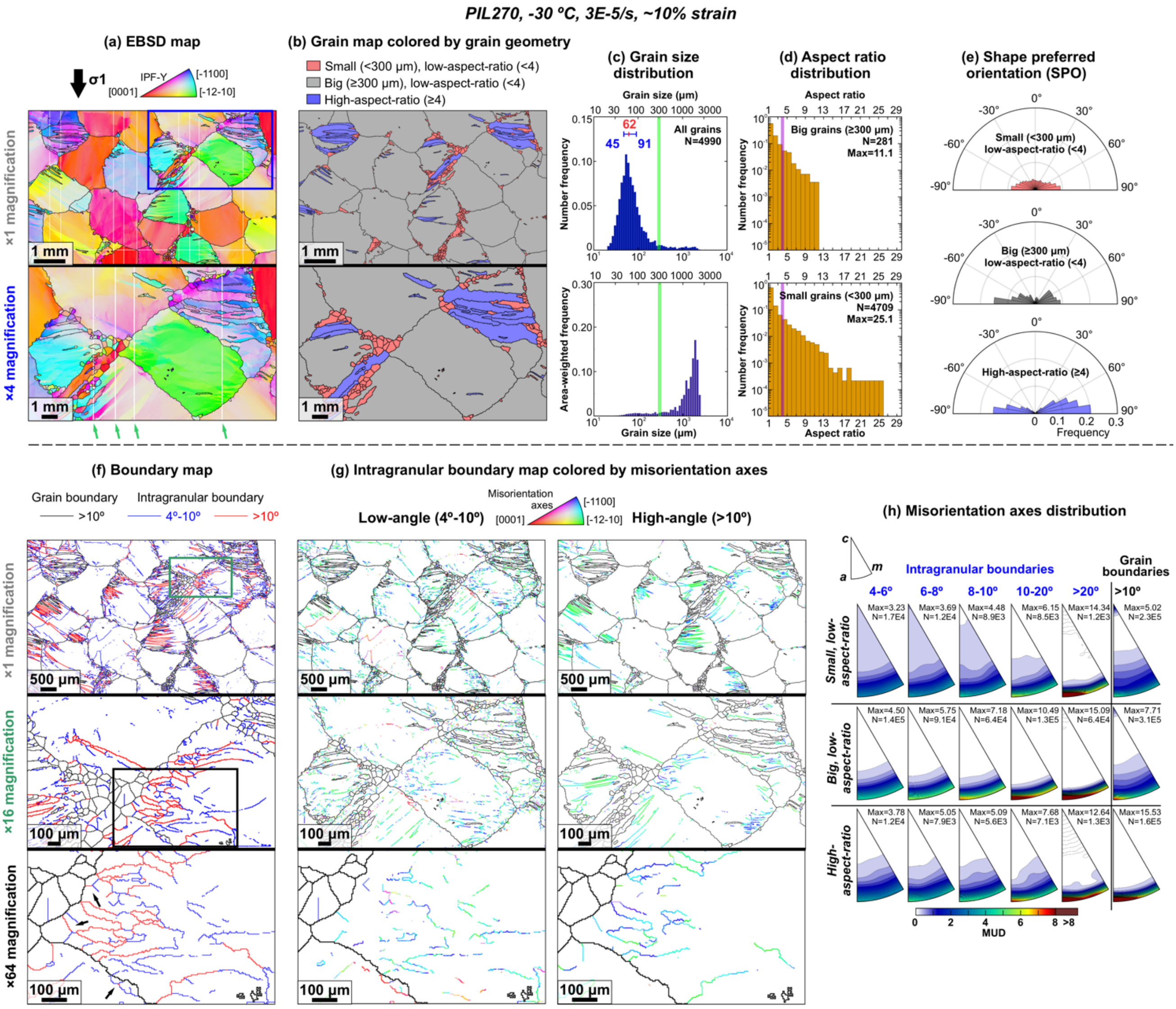

Figure 3. Microstructural analyses of sample PIL270. The descriptions of **(a)** to **(h)** are the same as in Fig. 2.

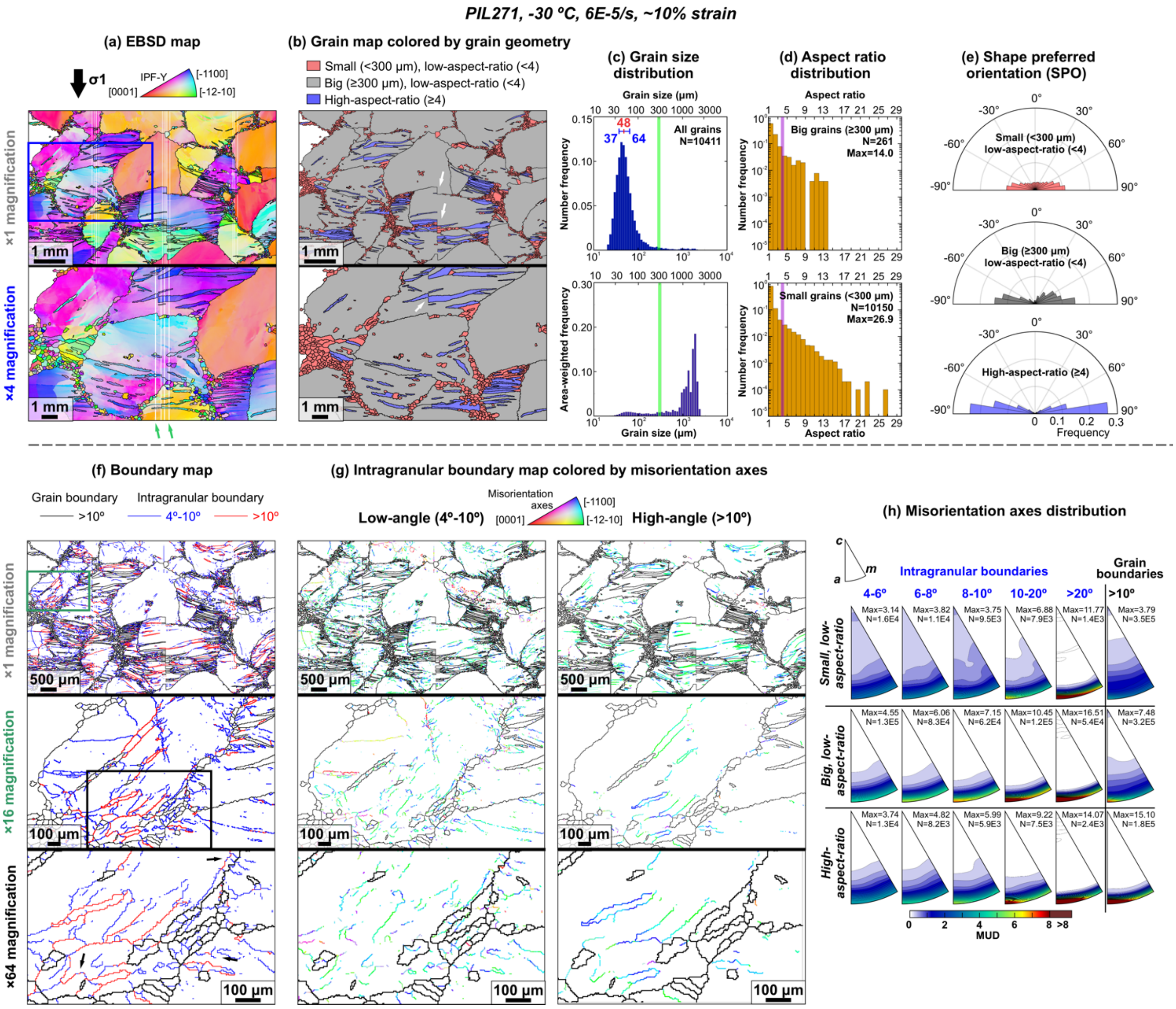

Figure 4. Microstructural analyses of sample PIL271. The descriptions of **(a)** to **(h)** are the same as in Fig. 2. The white arrows in (b) indicate artefacts of shift between adjacent tiles within montaged EBSD data (Sect. 2.4.1).

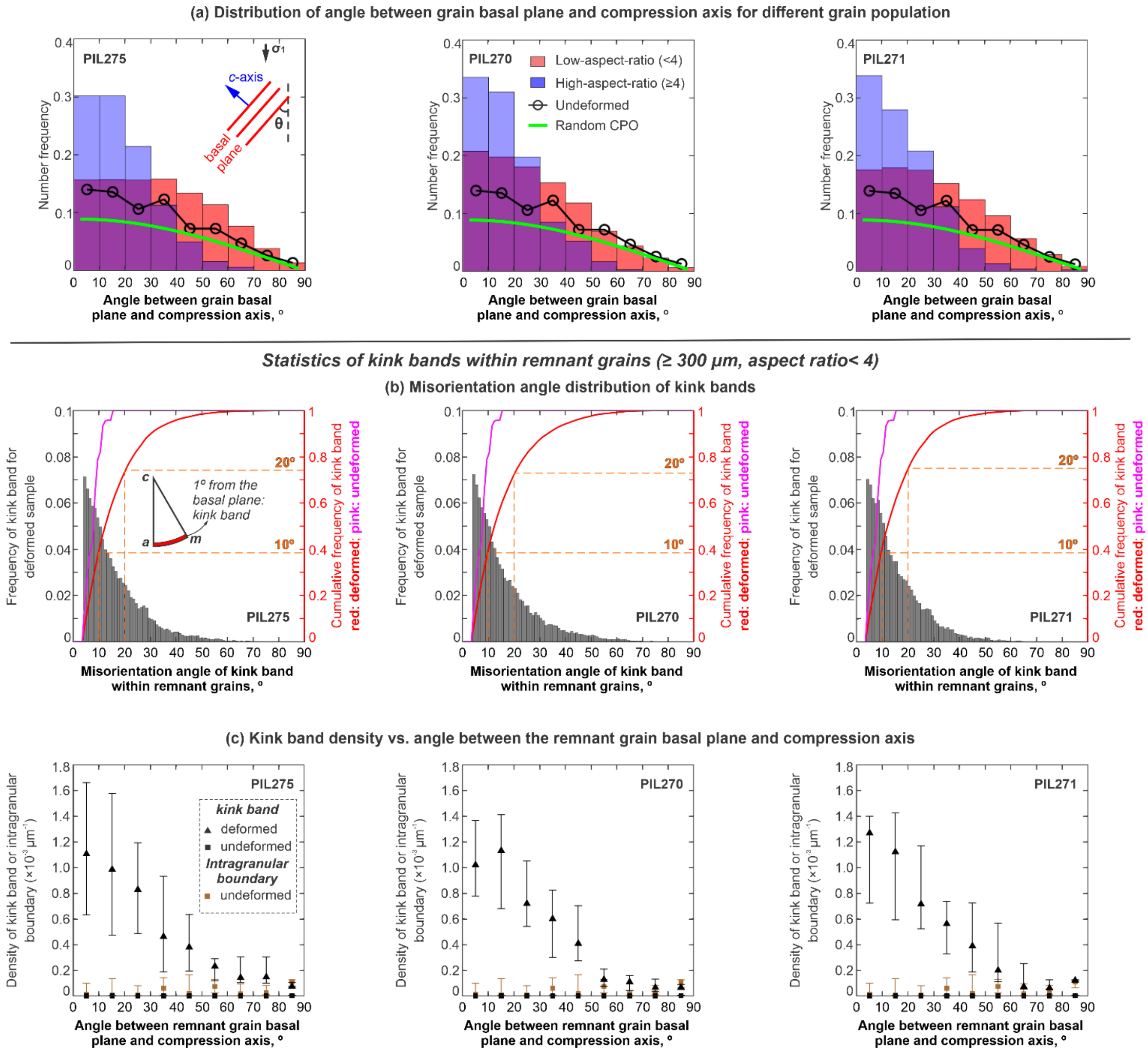

Figure 5. (a) Number frequencies of high- and low-aspect-ratio grains with basal planes at 10° intervals to the compression axis. **(b)** Bar plots (grey, corresponds to the left y-axis) represent misorientation angle distribution of kink band, i.e., intragranular boundary with misorientation axis within 1° to the ice basal plane, for deformed sample. Line plots (corresponds to the right y-axis) represent cumulative frequency of kink band as a function of misorientation angle for deformed sample (red) and undeformed sample (pink). **(c)** Distribution of kink band density as a function of the angle between basal plane and compression axis for remnant grains (≥ 300 μm, aspect ratio < 4) for deformed sample (black triangle). These data are compared with the kink band density (black square), i.e., the length of kink band per grain area, as well as intragranular boundary density (brown square), i.e., the length of intragranular boundary per grain area, of all grains within undeformed sample. Kink band and intragranular boundaries comprise low- (4°-10°) and high-angle (>10°) components. Distribution of kink band or intragranular boundary density is visualised as whiskers indicating lower quartile and higher quartile and a triangle or square indicating median value.

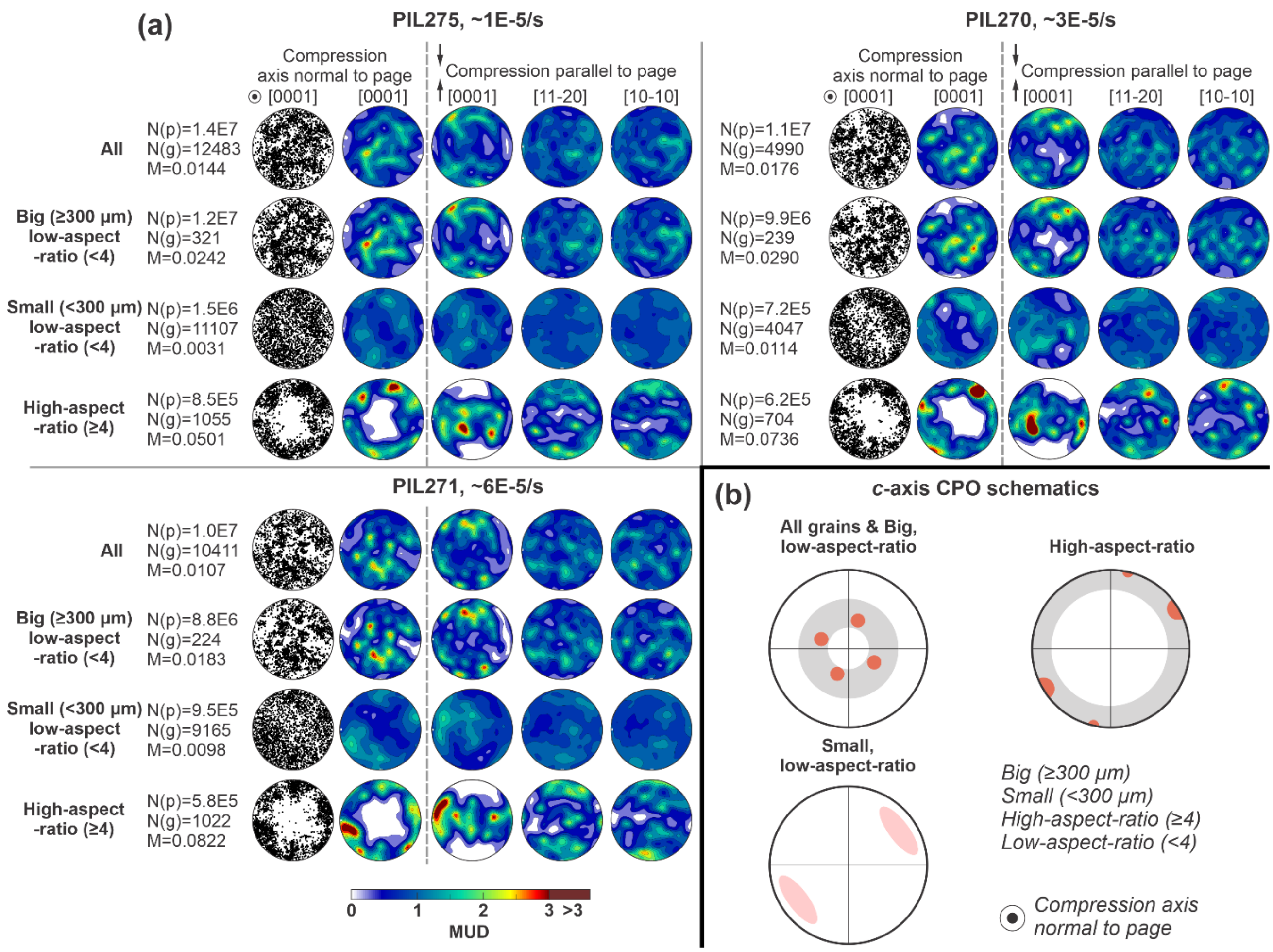

Figure 6. (a) Crystallographic preferred orientation (CPO) analyses using orientation data of all pixels for all grains and different grain populations. CPOs of different samples are presented in separate boxes. Within each box, the grain population name, grain number (N(g)), the number of pixels used for calculation (N(p)) and M-indices (M) are presented in the first column. The distributions of [0001] (*c*-axes) orientations plotted as point pole figures with 5000 randomly selected points and contoured pole figures are presented in the second and third column, respectively, with the compression axis perpendicular to page. The distributions of orientations for [0001] (*c*-axes), $[11\bar{2}0]$ *a*-axes and $[10\bar{1}0]$ (poles to the *m*-plane), with the compression axis vertical, are presented in the fourth, fifth and sixth column, respectively. **(b)** Summary of *c*-axis CPO schematics for different grain populations from (a).

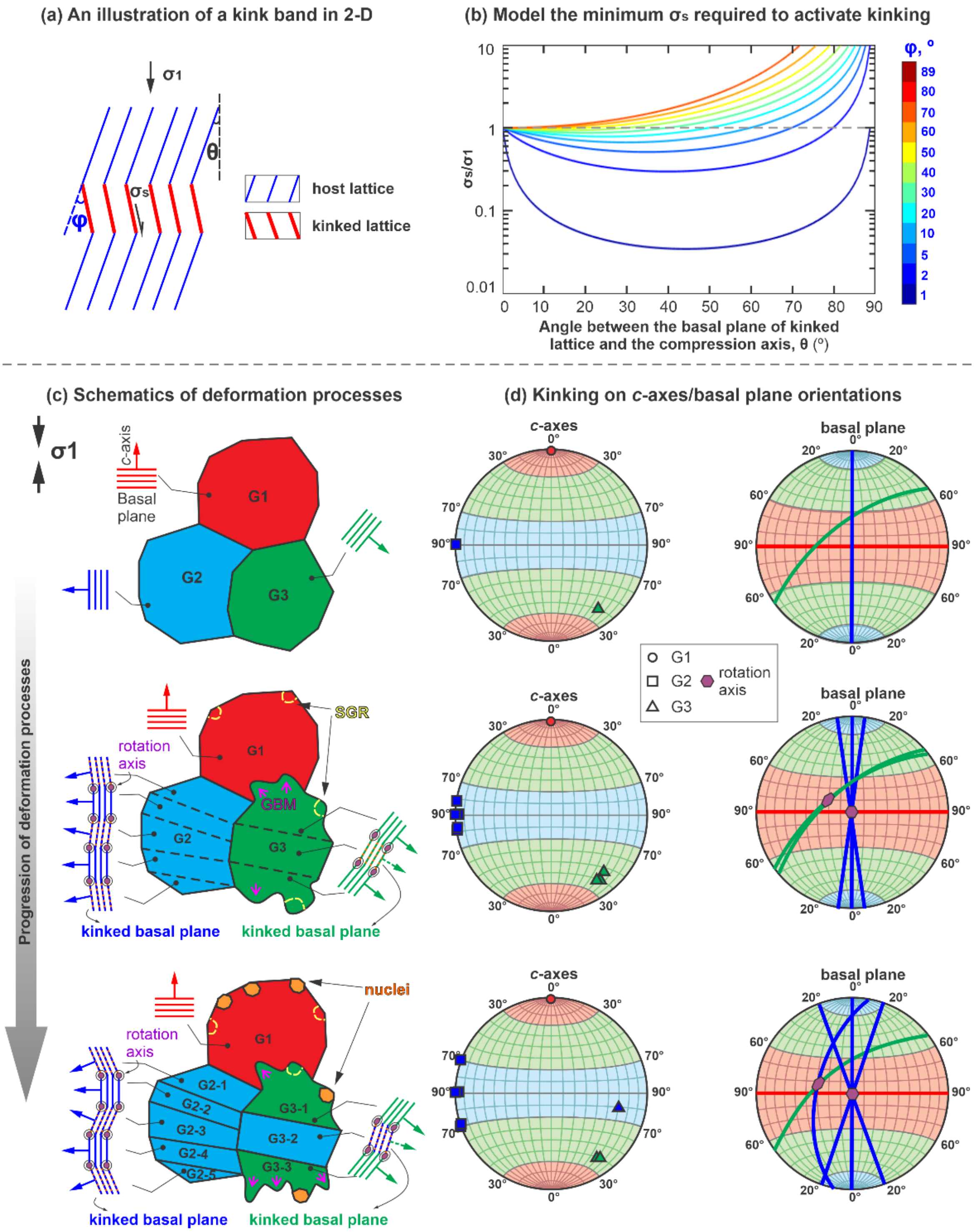

Figure 7. (a) Schematic drawing illustrating a kink band structure in 2-D. **(b)** Modelling results showing the minimum shear stress required for a kink band to continue with the deformation should be a function of the angle between the basal plane of host lattice and compression axis as well as the rotation angle of the kink band relative to the host lattice (Honea and Johnson, 1976; Nishikawa and Takeshita, 1999). **(c)** Schematic drawing of processes involved in the deformation of coarse-grained ice under uniaxial compression. GBM represents grain boundary migration; SGR represents subgrain rotation. For kinked lattices in **(c)**, we draw the corresponding orientations of *c*-axes and basal planes in pole figures in **(d)**.